Stability of Alkali-Seeded Hydrogen Arcjets *

Folusho Oyerokun† Darrel Robertson‡ and Manuel Martinez-Sanchez§
Massachusetts Institute of Technology
Cambridge, Massachusetts

A region of stable operation has been shown to exist for a Cesium seeded Hydrogen arcjet, in rough agreement with previous assumptions. Two electrothermal ionization instabilities were identified, one for the seed (at low electron temperatures) and one for the background gas, at $T_e \geq 8000\,K$. The latter, to be avoided in operation, was shown to occur whenever the Hydrogen dissociation fraction exceeds about 2%. Progress has been made on a detailed 2-D model, but results are still pending.

Nomenclature

E_{coll}	Rate per unit volume of electron-gas collisional energy transfer
$\vec{E}$	Electric field
$\vec{j}$	Current density
T, T_e	Temperature of gas and electrons
$K_f(T)$	Forward rate constant
$K_n(T)$	Molar equilibrium constant for H_2 dissociation
k_B	Boltzmann's constant
n_s	Number density of species s
P, P_t	Pressure (static, total)
$R(T_e)$	Recombination constant for H^+
$S_s(T_e)$	Saha function for species s
α	Seed fraction (by mole)
δ	Perturbation
κ_e, κ	Electronic and gas thermal conductivity
ν_{es}	Collision frequency of electrons with species s
δ_s	Inelastic collision correction factor
σ	Electrical conductivity
ϕ	Potential
C_v	Specific heat at constant volume
ϵ_{i_s}	First ionization energy of species s
ϵ_d	Dissociation energy of Hydrogen

Other symbols are defined in the text.

1 Introduction

The concept of introducing a small percentage of Cesium into a Hydrogen arcjet for the purpose of strongly reducing frozen losses was previous examined in Ref.[1]. It was shown there that specific impulses on the order of 900 seconds were feasible with negligible ionization and dissociation losses, and that the "arc" was in fact very diffuse, further improving performance. One major caveat remained after the work in Ref.[1], namely, the possibility of the sudden "ignition" of a conventional Hydrogen arcjet if conditions favored ionization of H atoms. Other issues needing better analysis were frictional losses in the generally long constrictor required, and perhaps other 2D effects, such as seed segregation.

In this work we report a linear stability analysis which supports the assumption of no H ionization adopted in [1]. We also report progress on the construction of a very detailed 2D model of the seeded arc, based on a previous pure Hydrogen model [2]. Results of this model were not yet available at the time of this writing.

2 Previous Work

The analysis in Ref.[1] was carried out with a quasi one-dimensional inviscid equilibrium constrictor flow model, coupled with a radial (Elenbaas-Heller) diffusion equation, modified to allow convective energy transport. The electrons were assumed to be maxwellized at a different temperature from the rest of the species. In order to suppress H ionization, the electron temperature was not allowed to exceed $7000K$. To minimize viscous losses, a restriction was also imposed on the channel length ($L/D \leq 10$). A Gaussian-like temperature distribution was specified at the inlet along with total pressure and Mach number. Other parameters specified were the arc current, seed fraction ratio, constrictor and cathode tip diameters. The constrictor wall was taken to be insulating. The coupled differential equations were simultaneously integrated downstream until the flow became choked. Arc attachment was assumed to occur at the choking point. Calculations based on frozen nozzle flow were then done to obtain the performance characteristics. Typical results obtained from the model for constrictor radius=$1.4\,mm$, cathode tip radius of $0.35\,mm$, and initial wall and core temperatures of $1000\,K$ and $3500\,K$ respectively are displayed in Table 1.

In order to identify trends in the numerical results, reference was made to a simple model of heat addition to a gas in a constant area duct, and the following approximate expressions for exit temperature and channel length were

†Graduate Student

‡Graduate Student

§Professor, AIAA Fellow

Table 1: Typical results obtained using the quasi 1D model

Seed (per mole)	3×10^{-4}			4×10^{-4}	
M_{inlet}	0.4	0.4	0.4	0.35	0.35
Current, A	17	15	12	15	17
Inlet P_{total}, atm	3.3	3	2.5	2.5	3
I_{sp}, sec	810	809	808	890	890
Voltage, V	384	658	410	432	457
Frozen Losses, %	0.24	0.2	0.4	4	3
L/D	5.8	11.3	9.6	9.2	8.3
Exit $T_{e_{max}}$	6304	4537	5462	6197	6122

obtained:

$$T_{t_{exit}} = \frac{T_{t_{inlet}}}{2(\gamma+1)M_0^2} \tag{1}$$

and

$$L = \frac{p_{t_0}\sigma}{(I/A)^2}\left(\frac{1}{2(\gamma+1)M_0} - M_0\right) \tag{2}$$

where A and I are the constrictor cross section area and arc current respectively.

Since the specific impulse is proportional to the exit temperature, a high enthalpy distribution at the inlet will boost it. This suggests some form of preheating, which can be done, for example, with a low power resistojet. However, frozen losses, due mainly to dissociation, are also a function of this temperature. A consequence of this dependence is the existence of a critical Mach number (from Eq.(1)) below which losses become large for a fixed inlet temperature distribution. Increasing the pressure decreases the degree of dissociation, but from equation (2) leads to an increase in the channel length, thereby incurring more viscous losses. Hence, it can be concluded that the only way of increasing the specific impulse is by raising the gas temperature, thus allowing more dissociation loss (but still avoiding the H ionization loss). However at higher degrees of dissociation, there is a concern that the assumption of only neutral Hydrogen may no longer be valid, since the probability of electron impact ionization increases with greater atom concentration. A direct result of this is the possibility of ionization instabilities appearing in this regime. The presence of such instabilities could lead to a transition to conventional Hydrogen arc operation.

3 Stability Analysis

The possibility of ionization instabilities is investigated by performing a stability analysis on the nonequilibrium governing equations. This analysis is carried out in a semi-infinite channel of width W. For mathematical convenience, a Cartesian coordinate system is chosen. The flow velocity and global pressure are taken to be uniform; their perturbations are also assumed negligible. For simplicity, Cesium atoms and ions are modeled in Saha equilibrium with the electrons. Neglecting convective terms, molecular ions, the effect of electron impact dissociation, energy invested in ionization and dissociation, and electron pressure gradients compared to Lorentz forces in the electron momentum equation, the relevant governing equations are

$$\frac{\partial n_{H^+}}{\partial t} = Rn_e\left(S_H n_H - n_e n_{H^+}\right) \tag{3}$$

$$\frac{n_e n_{C_s^+}}{n_{C_s}} = S_{C_s}(T_e) \tag{4}$$

$$n_{C_s} + n_{C_s^+} = \alpha(2n_{H_2} + n_H + n_{H^+}). \tag{5}$$

$$n_e = n_{H^+} + n_{C_s^+} \tag{6}$$

$$\frac{\partial n_H}{\partial t} = K_f(T)(5n_H + 2n_{H_2})\left(n_{H_2} - \frac{n_H^2}{K_n}\right) \tag{7}$$

$$-Rn_e\left(Sn_e - n_e n_{H^+}\right) \tag{8}$$

$$\vec{j} = \sigma\vec{E} \tag{9}$$

$$p = (n_H + n_{H_2})k_B T + n_e k_B(T_e + T) = const. \tag{10}$$

$$\frac{3}{2}n_e k_B\frac{\partial T_e}{\partial t} - \nabla\cdot(\kappa_e\nabla T_e) = \frac{j^2}{\sigma} - E_{coll} \tag{11}$$

$$\rho C_v\frac{\partial T}{\partial t} - \nabla\cdot(\kappa\nabla T) = E_{coll} \tag{12}$$

and

$$\nabla\cdot(\sigma\nabla\phi) = 0 \tag{13}$$

3.1 Linearization of the Governing Equations

The next step is to consider the response of the system to small wave-like perturbations in densities, temperatures and electric potential of the form:

$$n_s = n_s^0 + \delta n_s \tag{14}$$

$$T_s = T_s^0 + \delta T_s \tag{15}$$

$$\phi = \phi^0 + \delta\phi \tag{16}$$

for all the species, s, present. For ease of analysis, the following group of nondimensional parameters are introduced:

$$\tau = \frac{t}{t_D} \tag{17}$$

$$\hat{x} = \frac{x}{L_D} \tag{18}$$

$$\hat{y} = \frac{y}{L_D} \tag{19}$$

$$\tilde{n}_s = \frac{\delta n_s}{n_s} \tag{20}$$

$$\tilde{T}_s = \frac{\delta T_s}{T_s} \tag{21}$$

$$\tilde{\phi} = \frac{\delta\phi}{\phi} \tag{22}$$

$$\Theta = \frac{T_e}{T} \quad (23)$$

$$\Omega = \left(\frac{\epsilon_{i_H}}{k_B T_e} + \frac{3}{2}\right) \quad (24)$$

$$G = \left(\frac{\epsilon_{i_{C_s}}}{k_B T_e} + \frac{3}{2}\right) \quad (25)$$

$$\Gamma = \left(\frac{1}{2T} + \frac{\theta_d}{T^2} - \frac{\theta_v}{T^2}\frac{1}{e^{\left(\frac{\theta_v}{T}\right)} - 1}\right) \quad (26)$$

$$\hat{R}_i = R n_H S_H t_D \quad (27)$$

$$\hat{R}_d = \frac{K_f (5n_H + 2n_{H_2}) n_H t_D}{K_n} \quad (28)$$

$$D_g = \frac{\kappa t_D}{\rho C_v L^2} \quad (29)$$

$$\Lambda = \frac{E_{coll} t_D}{\rho C_v T} \quad (30)$$

$$\Xi = \frac{\epsilon_d n_H}{\rho C_v T} \quad (31)$$

$$C = \frac{T_e}{\nu_e}\frac{\partial \nu_e}{\partial T_e} \quad (32)$$

$$C^* = \frac{T_e}{\nu_e^*}\frac{\partial \nu_e^*}{\partial T_e} \quad (33)$$

where

$$\nu_e = \sum_s \nu_{es} \quad (34)$$

$$\nu_e^* = \sum_s \nu_{es}\delta_s \quad (35)$$

The Ohmic heating time, t_D, and the heat diffusion distance in time t_D are defined as

$$t_D = \left(\frac{\frac{3}{2} n_e k_B T_e \sigma}{j^2}\right) \quad (36)$$

$$L_D = \sqrt{\frac{\kappa_e t_D}{\frac{3}{2} n_e k_B}} \quad (37)$$

The reference potential is arbitrarily chosen to be

$$\phi = \frac{j L_D}{\sigma} \quad (38)$$

After linearization, the perturbation equations take the form:

$$\left(1 + \frac{n_{C_s^+}}{n_e + S_{Cs}}\right)\tilde{n}_e - \frac{n_{H^+}}{n_e}\tilde{n}_{H^+} - \frac{n_{C_s^+}}{n_e(2n_{H_2} + n_H)}$$
$$(n_H \tilde{n}_H + 2n_{H_2}\tilde{n}_{H_2}) - \frac{n_{C_s^+}}{n_e} G\left(1 - \frac{n_{C_s^+}}{\alpha(2n_{H_2} + n_H)}\right)\tilde{T}_e \quad (39)$$

$$\frac{\partial \tilde{n}_{H^+}}{\partial \tau} = \hat{R}_i\left(-\tilde{n}_e - \tilde{n}_{H^+} + \tilde{n}_H + \Omega \tilde{T}_e\right) \quad (40)$$

$$\frac{\partial \tilde{n}_H}{\partial \tau} = \hat{R}_i \frac{n_{H^+}}{n_H}\left(\tilde{n}_e + \tilde{n}_{H^+} - \Omega \tilde{T}_e\right)$$
$$- \left(2\hat{R}_d + \hat{R}_i \frac{n_{H^+}}{n_H}\right)\tilde{n}_H + \hat{R}_d\left(\tilde{n}_{H_2} + \Gamma \tilde{T}\right) \quad (41)$$

$$\frac{n_e}{n_{H_2}}(\Theta + 1)\tilde{n}_e + \frac{n_H}{n_{H_2}}\tilde{n}_H + \tilde{n}_{H_2} + \frac{n_e}{n_{H_2}}\Theta \tilde{T}_e$$
$$+ \frac{n_e + n_H + n_{H_2}}{n_{H_2}}\tilde{T} = 0 \quad (42)$$

$$\frac{\partial \tilde{T}_e}{\partial \tau} - \hat{\nabla}^2 \tilde{T}_e = -\left(\frac{\nu_{ei}}{\nu_e} + \frac{\nu_{ei}}{\nu_e^*}\right)\tilde{n}_e - \left(\frac{\nu_{eH}}{\nu_e} + \frac{\nu_{eH}}{\nu_e^*}\right)\tilde{n}_H$$
$$- \left(\frac{\nu_{eH_2}}{\nu_e} + \frac{\nu_{eH_2}}{\nu_e^*}\right)\tilde{n}_{H_2} + \left(C + \frac{\Theta}{\Theta - 1} + C^*\right)\tilde{T}_e \frac{\tilde{T}}{\Theta - 1}$$
$$- 2\frac{\partial \tilde{\phi}}{\partial \hat{x}} \quad (43)$$

$$\frac{\partial \tilde{T}}{\partial \tau} - D_g \hat{\nabla}^2 \tilde{T} = \Lambda\left[\left(1 + \frac{\nu_{ei}}{\nu_e^*}\right)\tilde{n}_e + \frac{\nu_{eH}}{\nu_e^*}\tilde{n}_H\right.$$
$$\left. + \frac{\delta_{H_2}}{2}\frac{\nu_{eH_2}}{\nu_e^*}\tilde{n}_{H_2} + \left(\frac{\Theta}{\Theta - 1} + C^*\right)\tilde{T}_e - \frac{\tilde{T}}{\Theta - 1}\right] \quad (44)$$

$$\hat{\nabla}^2 \tilde{\phi} - \left(1 - \frac{\nu_{ei}}{\nu_e}\right)\frac{\partial \tilde{n}_e}{\partial \hat{x}} - \frac{\nu_H}{\nu_e}\frac{\partial \tilde{n}_H}{\partial \hat{x}} - \frac{\nu_{H_2}}{\nu_e}\frac{\partial \tilde{n}_{H_2}}{\partial \hat{x}} - C\frac{\partial \tilde{T}_e}{\partial \hat{x}} \quad (45)$$

3.2 Dispersion Relations

As is usual in linear stability analysis, the disturbance is now decomposed into its Fourier components:

$$\tilde{n}_s = \hat{n}_s e^{i(\vec{k}\cdot\vec{r} - \omega\tau)} \quad (46)$$

$$\tilde{T}_s = \hat{T}_s e^{i(\vec{k}\cdot\vec{r} - \omega\tau)} \quad (47)$$

$$\tilde{\phi} = \hat{\phi} e^{i(\vec{k}\cdot\vec{r} - \omega\tau)} \quad (48)$$

where the hatted quantities are the complex amplitudes, and $\vec{k}$ and $\vec{r}$ are the wave and position vectors respectively. The quantity ω is the complex frequency:

$$\omega = \omega_r + i\,\omega_i \quad (49)$$

The wave vector is set to lie at an angle θ with the background current (x-axis), so that

$$\vec{k}\cdot\vec{r} = k\,(\hat{x}\cos\theta + \hat{y}\sin\theta) \quad (50)$$

As a result,

$$\frac{\partial}{\partial \tau} \rightarrow -i\omega \quad (51)$$

$$\frac{\partial}{\partial \hat{x}} \rightarrow ik\cos\theta \quad (52)$$

$$\frac{\partial}{\partial \hat{y}} \rightarrow ik\sin\theta \quad (53)$$

$$\hat{\nabla}^2 \rightarrow -k^2 \quad (54)$$

After Fourier decomposition, the linearized perturbation equations reduce to a system of homogeneous algebraic equations, for which the compatibility condition, although very complicated, can be written in the form:

$$k^2\left[f_1(w,k) + \cos^2(\theta)\, f_2(w,k)\right] = 0 \quad (55)$$

where f_1 is a polynomial of degree 4 in both ω and k, and f_2 is of second degree in both k and ω. The roots of equation (55) represent the different modes of propagation of the

disturbance. The sign of ω_i indicates the development of the perturbation in time: positive signifies growth, hence instability, while negative indicates a decaying stable mode. The general requirement of system stability is for all ω_i to be negative ($\omega_i = 0$ signifies marginal stability).

A close inspection of Equation (55) shows that ω_i is most positive (or least negative), when

$$k = 0 \tag{56}$$

$$\theta = \frac{\pi}{2} \tag{57}$$

Hence, it can be concluded that the least stable mode occurs at an angle $\frac{\pi}{2}$ between the wave vector and background current density, and at the maximum possible wavelength of propagation, which for practical purposes equals twice the channel width.

3.3 Results

In this subsection, the behavior of the system on variation of each of the background parameters is discussed for the extreme case $\vec{k} = 0$. Results obtained are not much different from that of the least stable (practical) mode.

Stability as a Function of Electron Temperature

Figure 1 shows the variation of the imaginary frequency of the least stable mode with electron temperature for $T = 2000K$, $P = 1atm$ and $\alpha = 3 \times 10^{-4}$. It can be inferred from the plot, that there are two regimes of instability: $T_e < 5630\,(T_{e_I})$ and $T_e > 8380\,(T_{e_{II}})$. These instabilities are ionizational (or electrothermal) in nature. An ionization instability occurs in regions of localized increase in electrical conductivity generally caused by fluctuations in densities and temperatures. Accompanying this is an increase in Joule dissipation due to current concentration in this region, which in turn fuels the electron temperature increase; hence, an instability ensues. This is confirmed in Figure 2 which shows $\tilde{\sigma}$ normalized against $\tilde{T}_e$ (i.e. $\tilde{\sigma}/\tilde{T}_e$) versus electron temperature. The nondimensional perturbation in electrical conductivity is given by

$$\tilde{\sigma} = \left(1 - \frac{\nu_{ei}}{\nu_e}\right)\tilde{n}_e - \frac{\nu_{eH}}{\nu_e}\tilde{n}_H - \frac{\nu_{eH_2}}{\nu_e}\tilde{n}_{H_2} - C\tilde{T}_e \tag{58}$$

In order to understand the mechanisms of these instabilities, consider a positive fluctuation in electron temperature ($\tilde{T}_e > 0$). From the gas temperature perturbation equation, Equation (44), it can be seen that this would lead to a corresponding increase in the gas temperature, hence, at constant pressure, a negative perturbation in the overall density. This fluctuation in electron temperature will also favor the ionization process in regions where the seed is not fully ionized. The direction of electron density perturbation therefore depends on which of the two effects (expansion and ionization) is stronger: positive in regions of strong ionization ($T_e \ll T_{e_I}$), and negative near the threshold, T_{e_I}. At low electron temperatures, Coulombic interactions tend to dominate because of the large electron ion collision cross section. Because the Coulomb collision frequency is inversely proportional to T_e, its partial derivative with electron temperature will be negative in this region, hence the nondimensional parameter $C < 0$. From Equation 58, it can be seen that the combination of these two effects at low T_e will lead to a positive fluctuation in conductivity, causing the system to go unstable. This trend continues until near full seed ionization where $\tilde{n}_e$ becomes negative. This coupled with the corresponding decrease in Coulombic interactions would result in stability being restored to the system. This argument is supported by Figure 3 which shows the variation of normalized $\tilde{n}_e/\tilde{T}_e$ and C with temperature around the transition region. The nonlinear evolution of this seed ionization instability would be self-limiting at some moderate core T_e, at which Cs reaches full ionization. Since this is well below $T_{e_{II}}$, where H ionization sets in, it should pose no problems.

As mentioned earlier, the perturbation in temperature of the gas goes in the same direction as that of the electrons. If the gas temperature is high enough, this positive fluctuation in gas temperature would favor the dissociation process, so that $\tilde{n}_{H_2} < 0$ and $\tilde{n}_H > 0$ (in the absence of H ionization). However, as the electron temperature approaches $T_{e_{II}}$, $\tilde{n}_H$ decreases and in fact, approaches zero around the threshold because of the ionization process. Figure 4 shows the variation of normalized $\tilde{n}_H$ (i.e $\frac{\tilde{n}_H}{\tilde{T}_e}$) with temperature in this region. As can be seen from Equation (58), this effect coupled with increase in $\tilde{n}_e$ would result in increase in conductivity and hence, an unstable ionization process. The nonlinear evolution of this instability would lead to strong constriction and core temperature elevation, eventually producing a thin, hot arc burning in hydrogen, as in pure Hydrogen arcjets.

Stability Behavior as a Function of Gas Temperature and Pressure

Illustrated in Figure 5 is a plot of background values of electron temperature against gas temperature at different pressures near the stability threshold. The lower plots represent the conditions below which the seed ionization instability occurs (mode I), while the second group corresponds to conditions above which Hydrogen ionization instability occurs (mode II). It can be seen from the plots that the electron temperature at which instabilities occur decreases with an increase in gas temperature. This is so, because an increase in dissociation occurs as gas temperature increases, hence there are more atoms of Hydrogen present for the electrons to ionize. An important observation made in the region of H ionization instability is that this instability typically occurs when electrons from Hydrogen atoms constitute about 2% of total. As seen from the plot, an increase in pressure delays the temperature at which the instabilities occur.

Stability Behavior as a Function of Cesium Seed Fraction

As mentioned earlier, the primary driving force for the first instability mode is the dominance of Coulombic interaction in this region. As a result, we expect this effect to disappear at conditions where the Coulombic interactions are not important. A comparison of the Coulomb collision frequency to that of $e - H_2$ shows that an approximate threshold condition is when

$$\frac{\nu_{ei}}{\nu_{eH_2}} \approx \frac{1.17 \times 10^{-9} \alpha ln\Lambda}{Q_{eH_2}(T_e)} \ll 1 \qquad (59)$$

From the above expression, we can estimate the electron temperatures below which seed ionization instability occurs for a given seed fraction, and vice versa. Some numerical examples based on this estimation are displayed in Table 2. These results are approximately confirmed by the lower plot in Figure 6 which shows the dependence of electron temperature on seed fraction at the stability threshold ($p = 1atm.$ and $T = 2000K$). The upper plot shows the dependence of $T_{e_{II}}$ versus the seed fraction. The reason why $T_{e_{II}}$ decreases with a corresponding decrease in seed fraction has to do with the increase in the proportion of electrons from atomic Hydrogen as the seed fraction decreases. It can be noticed, however, that the two temperatures, i.e T_{e_I} and $T_{e_{II}}$ approach each other at high seed fraction. The value at which this occurs is the upper bound on seed fraction, and results in a situation where the system is always unstable.

Table 2: Approximate values of electron temperature below which seed ionization instability occurs for a given seed fraction.

α	T_{e_I}
10^{-4}	2936
3×10^{-4}	4707
5×10^{-4}	5821
10^{-3}	7710
1.2×10^{-3}	8291

4 2D Numerical Model

4.1 Gas Physics

As noted, a separate effort is underway to generalize our analysis by allowing many other effects to be expected in a realistic seeded arcjet. Following is a description of the axisymmetric 2D model developed for this purpose.

A Cesium ion fluid was added to a two dimensional numerical model of a Hydrogen arcjet thruster[2], making it a three fluid model. The numerical model is axisymmetrical with flow variables in the azimuthal direction neglected, with the exception of swirl which is accounted for in the momentum equations.

The model accounts for Hydrogen in the forms H2, H, H+, and also electrons, and Cesium ions. Atomic Cesium has been initially neglected, since Cs is fully ionized over the most important portions of the flow; partial Cs ionization effects will be examined subsequently.

Due to its much larger mass than Hydrogen the Cesium ions would be expected to diffuse much more slowly, and due to the swirl may be centrifugally pushed outwards. To properly follow the flow of Cesium ions they were modelled as a separate species, as also were the electrons on account of their much lighter mass. The Hydrogen species were assumed to be in translational thermal equilibrium with one another and share a common temperature and are modelled together as a single fluid.

With charged species present electrodynamic effects must be accounted for. This is done by imposing zero current divergence and relating current to potential and pressure gradients through Ohm's law (magnetic effects are neglected). Quasineutrality is assumed in all regions of the flow except within the sheaths.

The evolution of the flow is determined by the conservation of mass, momentum, and energy, giving five equations for each fluid to be modelled. The internal energy form of the energy equation was used since Miller[2] found that the strong form was not suitable for arcjet simulation. Dissociation and ionization were treated as non-equilibrium processes so that there was a finite rate of production of atomic and ionized Hydrogen. Sheppard's [3] recombination rate coefficient was used since it is valid for electron temperatures up to 60000 K whereas the assumptions on which the Hinnov-Hirschberg coefficient are based break down above 3000 K. Each component was assumed to obey the ideal gas law, and for the transport properties, since mean free path arguments are only accurate to a factor of two, the Chapman-Enskog solution was used. The correct solution to the transport coefficients in a mixture of fluids is computationally intensive, so simpler mixture rules based on mean free path arguments were used. Electrons diffuse much more quickly than ions, and set up a charge separation electric field, which accelerates the ions and slows the electrons. Ambipolar diffusion, as was assumed for the model, is where there is no net current due to charge separation. This concept was generalized to the multi-ion situation potentially occurring here.

4.2 Boundary conditions

The inlet was assumed to be a plenum with a specified mass flow injected through a large number of evenly spaced holes so the inlet flow was subsonic and parallel to the walls. Swirl was injected as a vortex with a velocity of about thirty percent of the total inlet velocity, and although assumed constant in the azimuthal direction was allowed to develop in the axial and radial directions. Outlet conditions were extrapolated from interior points for the case of supersonic outflow, and calculated using Riemann invariants for subsonic outflow regions. For the flow symmetry line the radial and azimuthal velocities were set to zero, and zero gradient imposed on all other quantities. Thruster walls had viscous no-slip conditions imposed on the velocities, and zero gradient normal to the wall on

all other quantities except for the densities, which were determined from sheath boundary conditions, by postulating a balance between the flux arriving at the plasma sheath boundary by diffusion, and the flux arriving at the wall by virtue of their thermal energy, assuming an electrostatically choked sheath. The surface was assumed to be catalytic for recombination and reflective for molecules. Miller's work showed that there was minimal effect on the flow inside the thruster if a self-consistent heat balance between the flow and walls was incorporated, so this was neglected, and the temperature profile along the walls was fixed.

4.3 Numerical Scheme

The multi-fluid flow was modelled as modified compressible Navier-Stokes equations which was solved numerically by MacCormack's predictor corrector scheme, and the elliptical equation for the electric potential was solved by successive over relaxation. Structured grids for the plasma flow and the electric potential were generated by Poisson's equation with grid control to provide extra resolution at the walls and in the core flow, with special attention paid to the cathode tip region. The grids were then transformed to a Cartesian mesh in the computational domain. For potential calculations in the region just downstream of the cathode tip a separate finer grid was used to cope with the high gradients.

Unfortunately, numerical problems have not yet been completely resolved, and converged $2D$ solutions cannot be reported at this time.

5 Conclusions

The arcjet seeding concept continues to appear physically viable, with a suitable region of stable operation, free of snap-over to a constricted Hydrogen arc regime. More work is required to analytically verify these results, before any test work is attempted.

References

[1] Oyerokun, F. and Martinez-Sanchez, M., "A Study of Alkali-Seeded Hydrogen Arcjet Performance," IEPC 95-236, 24th International Electric Propulsion Conference, Moscow, Russia, 1995.

[2] Miller, S. A. and Martinez-Sanchez, M., "Nonequilibrium Numerical Simulation of Radiation-Cooled Arcjet Thrusters," IEPC 93-219, 23rd International Electric Propulsion Conference, Seattle, 1993.

[3] Sheppard, E. J., *Ionization Nonequilibrium and Ignition in Plasma Accelerators*, Doctoral Thesis, Massachusetts Institute of Technology, 1994.

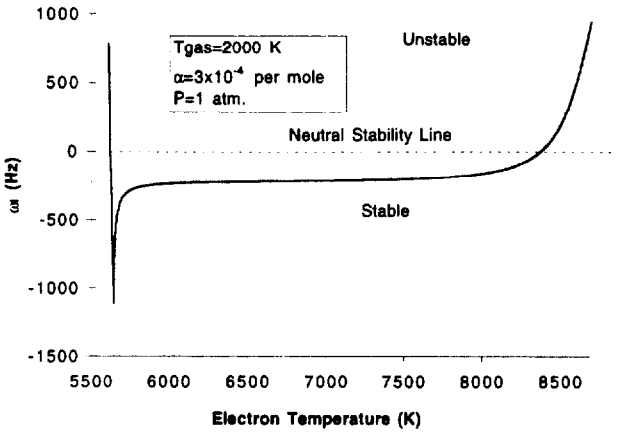

Figure 1: Imaginary frequency vs electron temperature.

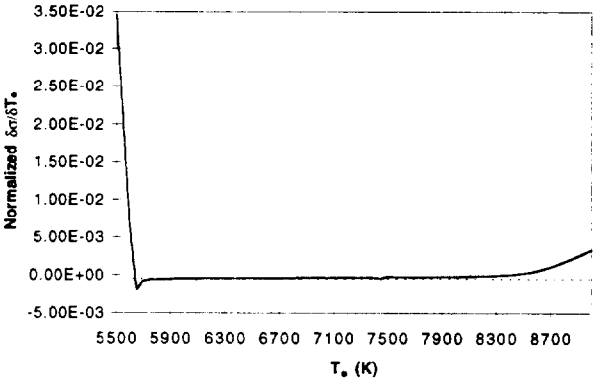

Figure 2: Relative perturbation in conductivity versus electron temperature.

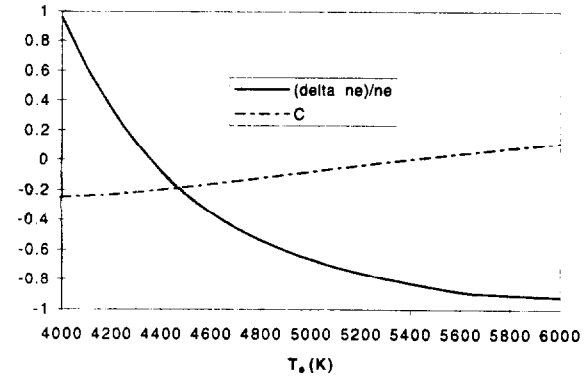

Figure 3: Electron density perturbation and nondimensional parameter C versus electron temperature.

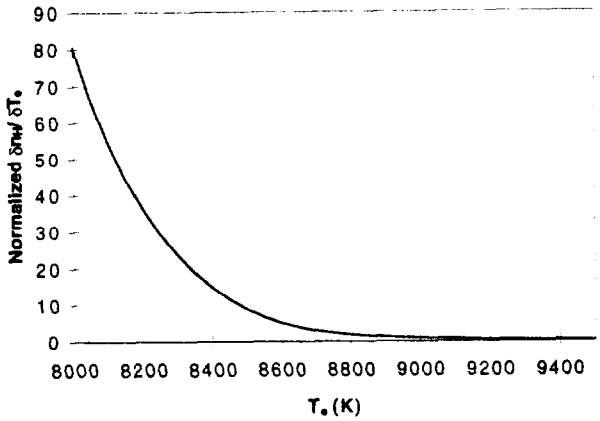

Figure 4: Atomic Hydrogen density perturbation versus electron temperature.

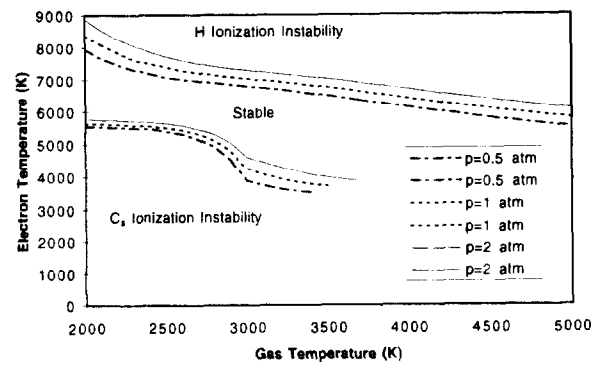

Figure 5: Threshold values of electron temperature versus gas temperature at different pressures.

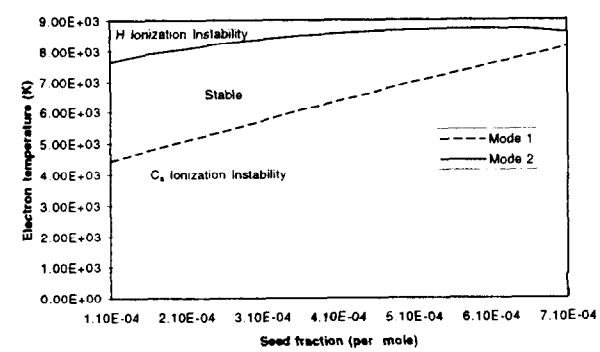

Figure 6: Threshold values of electron temperature versus Cesium seed fraction.